

A Stable 1D Multigroup High-Order Low-Order Method

B. C. Yee, A. B. Wollaber, T. S. Haut & H. Park

To cite this article: B. C. Yee, A. B. Wollaber, T. S. Haut & H. Park (2016): A Stable 1D Multigroup High-Order Low-Order Method, Journal of Computational and Theoretical Transport, DOI: [10.1080/23324309.2016.1187172](https://doi.org/10.1080/23324309.2016.1187172)

To link to this article: <http://dx.doi.org/10.1080/23324309.2016.1187172>



Published online: 13 Jul 2016.



Submit your article to this journal [↗](#)



Article views: 56



View related articles [↗](#)



View Crossmark data [↗](#)

A Stable 1D Multigroup High-Order Low-Order Method

B. C. Yee^{a,b}, A. B. Wollaber^a, T. S. Haut^a, and H. Park^a

^aComputational Physics and Methods Group (CCS-2), Los Alamos National Laboratory, Los Alamos, NM, USA; ^bDepartment of Nuclear Engineering and Radiological Sciences, University of Michigan, Ann Arbor, MI, USA

ABSTRACT

The high-order low-order (HOLO) method is a recently developed moment-based acceleration scheme for solving time-dependent thermal radiative transfer problems, and has been shown to exhibit orders of magnitude speedups over traditional time-stepping schemes. However, a linear stability analysis by Haut et al. (2015) revealed that the current formulation of the multigroup HOLO method was unstable in certain parameter regions. Since then, we have replaced the intensity-weighted opacity in the first angular moment equation of the low-order (LO) system with the Rosseland opacity. This results in a modified HOLO method (HOLO-R) that is significantly more stable.



This paper has two primary components. First, we present results from a linear stability analysis of the HOLO-R method for a 2-group problem. These results show that HOLO-R is stable in all regions of the parameter space we considered, and strongly suggest that HOLO-R is unconditionally stable. The predicted decay factors from the stability analysis are verified with numerically computed decay factors from a spectral HOLO-R code. Second, we describe a preliminary (unoptimized) implementation of HOLO-R in Capsaicin – a deterministic, discrete-ordinates radiation transport code at Los Alamos National Laboratory. The results from this implementation further verify the stability of the HOLO-R method. Moreover, in the simulation of a 50-group, nonlinear Marshak wave problem, away from the 2-group, linearized stability analysis, we assess HOLO-R's accuracy, efficiency, and robustness as compared to current methods in Capsaicin. To our knowledge, this is the first implementation of HOLO that uses a mass-lumped discontinuous Galerkin spatial discretization for both the high-order (HO) and LO systems, and details of this discretization are provided in the Appendix.

KEYWORDS

Discontinuous Galerkin;
high-order low-order
(HOLO); stability analysis;
thermal radiative transfer

1. Introduction

The thermal radiative transfer (TRT) equations describe the interaction of photons with surrounding media. They consist of two primary equations: A transport equation that describes the evolution of the radiation field, and a material energy

CONTACT B. C. Yee  bcyee@umich.edu  Computational Physics and Methods Group (CCS-2), Los Alamos National Laboratory, Los Alamos, NM, USA.

Color versions of one or more of the figures in the article can be found online at www.tandfonline.com/ltty.

© 2016 Taylor & Francis Group, LLC

balance equation that describes the evolution of the temperature of the surrounding media.

For 1D multigroup problems without scattering, the two equations can be written as

$$\frac{1}{c} \frac{\partial I_{g,m}}{\partial t}(x, t) + \mu_m \frac{\partial I_{g,m}}{\partial x}(x, t) + \sigma_g(T) I_{g,m}(x, t) = 2\pi \sigma_g(T) B_g(T), \quad (1)$$

$$c_v \frac{\partial T}{\partial t}(x, t) + \sum_{g=1}^G \sigma_g(T) \sum_{m=1}^M I_{g,m}(x, t) w_m = \sigma_P(T) a c T^4. \quad (2)$$

Here, we have also used the discrete ordinates (S_N) approximation. $I_{g,m}(x, t)$ is the space- and time-dependent angular intensity in direction μ_m integrated over energy group g , $T(x, t)$ is the material temperature, $\sigma_g(T)$ is the temperature-dependent group- g opacity (between group boundaries ν_{g-1} and ν_g), G is the total number of groups,

$$B_g(T) \equiv \int_{\nu_{g-1}}^{\nu_g} d\nu B(\nu, T) = \int_{\nu_{g-1}}^{\nu_g} d\nu \frac{2\nu^3}{c^2 h^3 [e^{\nu/T} - 1]}, \quad (3)$$

and σ_P is the Planck-weighted opacity, defined by

$$\sigma_P(T) \equiv \frac{\sum_{g=1}^G \sigma_g(T) B_g(T)}{\sum_{g=1}^G B_g(T)} = \frac{4\pi \sum_{g=1}^G \sigma_g(T) B_g(T)}{a c T^4}. \quad (4)$$

a , c , h , and c_v are constants representing the radiation constant, the speed of light, Planck's constant, and the specific heat of the material, respectively. a is also given by

$$a = \frac{8\pi^5}{15c^3 h^3}. \quad (5)$$

The TRT equations are nonlinear in temperature, and the numerical integration of these equations generally requires a semi-implicit or better time-stepping method for stability. Backward Euler time discretizations of Equations (1) and (2) are given by

$$\frac{I_{g,m}^{n+1}(x) - I_{g,m}^n(x)}{c\Delta t} + \mu \frac{\partial I_{g,m}^{n+1}}{\partial x}(x) + \sigma_g(T^{n+1}) I_{g,m}^{n+1}(x) = 2\pi \sigma_g(T^{n+1}) B_g(T^{n+1}), \quad (6)$$

$$\frac{c_v}{\Delta t} [T^{n+1}(x) - T^n(x)] + \sum_{g=1}^G \sigma_g(T^{n+1}) \sum_{m=1}^M I_{g,m}^{n+1}(x) w_m = \sigma_P(T^{n+1}) a c [T^{n+1}(x)]^4. \quad (7)$$

Here, $I_{g,m}^n$ is the angular flux in direction μ_m at time step n , integrated over energy group g . Although using an implicit time-stepping method leads to stability and ensures that I and T satisfy a maximum principle (Larsen et al., 2013), solving Equations (6) and (7) for I^{n+1} and T^{n+1} can be prohibitively costly due to the high dimensionality and nonlinearity of these equations.

Significant research has gone into developing methods for solving the TRT equations that are both stable and efficient. A standard method for solving the TRT equations over the past few decades has been the Implicit Monte Carlo (IMC) method (Fleck and Cummings, 1971). Through a linearization process, IMC introduces an “effective scattering” term that models the absorption and re-emission of photons within a time step. Although this method provides significantly more stability than explicit time-discretizations, it can be slow when the parameters deviate far from the point about which the linearization is done. Moreover, it is not a fully implicit method and can produce inaccurate and unphysical solutions at large time steps (Wollaber et al., 2013). There are alternative linearizations besides the IMC equations that may be solved deterministically, but these linearizations suffer the same inaccuracies for larger time steps (Wollaber, 2016). Alternatively, it is possible to deterministically solve the nonlinear, implicit TRT equations to overcome these accuracy limitations at concomitant expense (see Nowak and Nemanic, 1999; Rathkopf et al., 2000, and the “hidalgo” approach in this article for examples). In this article, we consider both linearized, semi-implicit and nonlinear, fully implicit solution approaches for the TRT equations.

Recently, Park et al. (2012, 2013, 2014, 2015) developed a high-order low-order (HOLO) method that allows for the efficient numerical integration of the TRT equations at large time steps. The gray low-order (LO) system consists of the material energy balance equation and the first two angular moments of the transport equation, while the high-order (HO) system consists of a multigroup transport equation whose Planckian emission source is computed from the LO system. In the predictor-corrector version of the method, the LO system is used to predict T^{n+1} . This predicted value is fed into the HO system, which produces updated intensity-weighted opacities and consistency terms. These HO quantities are then fed back into the LO system for a corrector step that produces the final values for time step $n + 1$. Results have shown orders of magnitude improvement in efficiency over traditional methods such as IMC. However, instabilities have occurred in recent attempts to apply the HOLO method to 2D problems. Moreover, a recent linear stability analysis by Haut et al. (2015) indicated that the multigroup HOLO method, as described in Park et al. (2014), can be unstable for 1D problems with a multigroup HO system and a gray LO system.

In this paper, we introduce and analyze the linear stability characteristics of HOLO-R, a modified version of the HOLO method that appears to be unconditionally stable for 1D problems with a multigroup HO system and a gray LO system. The primary difference between HOLO-R and HOLO is that HOLO-R uses the Rosseland opacity instead of the intensity-weighted opacity in the 1st angular moment equation of the LO system. We also discuss, but do not fully examine, several alternatives to HOLO-R that we initially considered that are likely more accurate away from thermal equilibrium. In particular, our analysis indicates that unconditional stability is achieved for problems near thermal equilibrium if the Rosseland opacity is employed; away from this limit, more accurate frequency- and angle-collapsed opacities could again be considered.

We organize the remainder of this paper as follows. [Section 2](#) will present the full algorithm for the HOLO-R method, note the differences between HOLO-R and HOLO, and discuss potential alternatives to using the Rosseland opacity. In [Section 3](#), we perform a linear stability analysis for the new HOLO-R method in the same manner that Haut did for the original HOLO method. Here, we show that it is now stable for all regions of the parameter space we considered – this includes all of the regions that Haut found to be unstable with the original HOLO method. Moreover, we verify the predicted decay factors from the stability analysis using a spectral HOLO code. [Section 4](#) will briefly describe the implementation of the HOLO-R method in the Capsaicin code at Los Alamos National Laboratory. In Capsaicin, both the HO and LO systems of HOLO-R are spatially discretized with a mass-lumped discontinuous Galerkin (DG) scheme. This section will also provide numerical results that (1) confirm the stability of HOLO-R suggested by the linear stability analysis, and (2) explore the accuracy and cost of the HOLO-R method as a function of the time step size and the number of HOLO iterations per time step. Lastly, in [Appendix A](#), we provide the full details of the spatial discretization of HOLO-R in Capsaicin.

2. The HOLO-R method

2.1. Algorithm

For a 1D, multigroup, S_N problem without scattering, the spatially continuous predictor-corrector HOLO-R method can be described by the following algorithm.

1. (LO predictor step) Solve for $E^{n+1/2}$, $F^{n+1/2}$, and $T^{n+1/2}$ using

$$\frac{E^{n+1/2} - E^n}{\Delta t} + \frac{\partial F^{n+1/2}}{\partial x} + c\sigma_E^n E^{n+1/2} = \sigma_P^n ac[T^{n+1/2}]^4, \quad (8)$$

$$\frac{F^{n+1/2} - F^n}{c\Delta t} + \frac{c}{3} \frac{\partial E^{n+1/2}}{\partial x} + \sigma_R^n F^{n+1/2} = \gamma^n E^{n+1/2}, \quad (9)$$

$$c_v \frac{T^{n+1/2} - T^n}{\Delta t} + ac\sigma_P^n [T^{n+1/2}]^4 = c\sigma_E^n E^{n+1/2}, \quad (10)$$

where E^n , F^n , and T^n represent the energy density, flux, and temperature from the previous time step n , respectively. The quantities σ_P^n , σ_E^n , σ_R^n , and γ^n are defined by

$$\sigma_E^n \equiv \frac{\sum_{g=1}^G \sigma_g(T^n) E_{HO,g}^n}{\sum_{g=1}^G E_{HO,g}^n} = \frac{\sum_{g=1}^G \sigma_g(T^n) E_{HO,g}^n}{E_{HO}^n}, \quad (11)$$

$$\sigma_P^n \equiv \frac{\sum_{g=1}^G \sigma_g(T^n) B_g(T^n)}{\sum_{g=1}^G B_g(T^n)}, \quad (12)$$

$$\sigma_R^n \equiv \frac{\sum_{g=1}^G \frac{\partial B_g}{\partial T}(T^n)}{\sum_{g=1}^G \frac{1}{\sigma_g(T^n)} \frac{\partial B_g}{\partial T}(T^n)}, \quad (13)$$

$$\gamma^n \equiv \frac{1}{E_{HO}^n} \left[\frac{F_{HO}^n - F_{HO}^{n-1}}{c\Delta t} + \frac{c}{3} \frac{\partial E_{HO}^n}{\partial x} + \sigma_R^n F_{HO}^n \right]. \quad (14)$$

$B_g(T^n)$ is defined by Equation (3) above, and E_{HO}^n , $E_{HO,g}^n$, and F_{HO}^n are quantities to be defined in the HO step below.

2. (HO step) With $B_g(T^{n+1/2})$ from the predictor step, solve for $I_{g,m}^{n+1}$ using

$$\frac{I_{g,m}^{n+1} - I_{g,m}^n}{c\Delta t} + \mu_m \frac{\partial I_{g,m}^{n+1}}{\partial x} + \sigma_g(T^n) I_{g,m}^{n+1} = \sigma_g(T^n) B_g(T^{n+1/2}). \quad (15)$$

$I_{g,m}^{n+1}$ is then used to generate the following quantities:

$$E_{HO,g}^{n+1} \equiv \frac{1}{c} \sum_{m=1}^M w_m I_{g,m}^{n+1}, \quad (16)$$

$$E_{HO}^{n+1} \equiv \sum_{g=1}^G E_{HO,g}^{n+1}, \quad (17)$$

$$F_{HO}^{n+1} \equiv \sum_{g=1}^G \sum_{m=1}^M w_m \mu_m I_{g,m}^{n+1}. \quad (18)$$

3. (LO corrector step) Finally, we solve for E^{n+1} , F^{n+1} , and T^{n+1} using

$$\frac{E^{n+1} - E^n}{\Delta t} + \frac{\partial F^{n+1}}{\partial x} + c\sigma_E^{n+1/2} E^{n+1} = \sigma_P^{n+1/2} ac[T^{n+1}]^4, \quad (19)$$

$$\frac{F^{n+1} - F^n}{c\Delta t} + \frac{c}{3} \frac{\partial E^{n+1}}{\partial x} + \sigma_R^{n+1/2} F^{n+1} = \gamma^{n+1/2} E^{n+1}, \quad (20)$$

$$c_v \frac{T^{n+1} - T^n}{\Delta t} + ac\sigma_P^{n+1/2} [T^{n+1}]^4 = c\sigma_E^{n+1/2} E^{n+1}, \quad (21)$$

where $\sigma_P^{n+1/2}$, $\sigma_E^{n+1/2}$, $\sigma_R^{n+1/2}$, and $\gamma^{n+1/2}$ are given by

$$\sigma_E^{n+1/2} \equiv \frac{\sum_{g=1}^G \sigma_g(T^n) E_{HO,g}^{n+1}}{E_{HO}^{n+1}}, \quad (22)$$

$$\sigma_P^{n+1/2} \equiv \frac{\sum_{g=1}^G \sigma_g(T^n) B_g(T^{n+1/2})}{\sum_{g=1}^G B_g(T^{n+1/2})}, \quad (23)$$

$$\sigma_R^{n+1/2} \equiv \frac{\sum_{g=1}^G \frac{\partial B_g}{\partial T}(T^{n+1/2})}{\sum_{g=1}^G \frac{1}{\sigma_g(T^n)} \frac{\partial B_g}{\partial T}(T^{n+1/2})}, \quad (24)$$

$$\gamma^{n+1/2} \equiv \frac{1}{E_{HO}^{n+1}} \left[\frac{F_{HO}^{n+1} - F_{HO}^n}{c\Delta t} + \frac{c}{3} \frac{\partial E_{HO}^{n+1}}{\partial x} + \sigma_R^{n+1/2} F_{HO}^{n+1} \right]. \quad (25)$$

We note that the opacities in Equations (22)–(25) are evaluated at the explicit temperature (T^n) rather than the predicted temperature ($T^{n+1/2}$). As such, the $n + 1/2$ superscript does not represent a true half-time step. This use of the explicit temperature instead of the predicted temperature is discussed in the paragraphs below.

In this HOLO-R algorithm, the first and last of the three LO equations are exact when the spatial variable is treated continuously. The former is obtained by taking the zeroth angular moment of the HO transport equation, while the latter is the material energy balance equation. The second equation of the LO system is exact if the consistency term is converged to the correct value. The consistency term accounts for the fact that we replaced $\sum_g \sigma_g F_g$ and the Eddington factor with $\sigma_R F$ and $\frac{1}{3}$, respectively. When the HOLO method is discretized in space, the consistency term also accounts for inconsistencies between the spatial discretizations of the HO and LO systems.

The HOLO-R method is nearly identical to the original HOLO method. The primary difference is that σ_R is now used in the first angular moment equation of the LO system instead of σ_E . As we will show in Section 3.2, this appears to make HOLO-R unconditionally stable.

Less significant differences also exist in the evaluation of the opacities for the LO system. The HOLO-R method in this paper evaluates all the opacities in the LO system using the explicit temperature (i.e., T^n , the temperature at the beginning of the current time step). In recent unpublished investigations, it was seen that, in the opacity evaluations for the corrector system, using the explicit temperature instead of the predicted temperature resulted in improved stability for difficult 2D problems. However, these investigations were for the original HOLO method. It is possible that this is no longer an issue with the HOLO-R method and that using an updated temperature can yield tangible improvements in accuracy. Previous work has briefly explored the updating of the temperatures in the opacity definitions (Park et al., 2014), but more work needs to be done to optimize these opacity definitions.

Finally, we note that the above ansatz represents a predictor-corrector version of the HOLO-R method. One can also improve the accuracy of the method by iterating between the HO and LO solutions to converge the consistency terms. The stability analysis will only be done on the predictor-corrector version of the method, but neither this work nor previous work has seen any signs of instability from iterating between the HO and LO systems. The effect of iterating between HO and LO on the accuracy of the solution will be explored briefly in Section 4.2.2.

2.2. Possible alternatives to σ_R

In the first angular moment of the energy-integrated transport equation, the collision term ($\sigma_g I_{g,m}$) has the form $\sum_{g=1}^G \sigma_g F_g$. Ideally, this should be represented in the 1-group setting with a flux-weighted opacity in a manner analogous to σ_E :

$$\sigma_F \equiv \frac{\sum_{g=1}^G \sigma_g F_g}{\sum_{g=1}^G F_g}. \quad (26)$$

From preliminary tests, using σ_F appears to yield a stable HOLO method, which is expected due to the consistency between the definition of σ_F and the HO system. However, unless the flux vector F_g maintains a fixed energy shape as it approaches 0, σ_F does not have a well-defined limit as $F_g \rightarrow 0$. Furthermore, even if F_g were to maintain a fixed energy shape as it approached 0, this energy shape would be a problem-dependent quantity that is generally not known beforehand. This creates serious robustness concerns since we cannot generally predict the numerical value of σ_F as $F_g \rightarrow 0$. Additionally, quantities such as F_g that contain canceling (positive/negative) tally contributions are more susceptible to statistical noise. Because of these concerns, previous HOLO methods have simply used σ_E , which is well defined but results in instability. Finally, we note that, in a multidimensional setting, F is a vector quantity and Equation (26) must be written component wise or otherwise adjusted.

As an alternative to σ_F , one may consider the use of partial flux weighted opacities σ_F^\pm , which are defined so that

$$\sum_{g=1}^G \sigma_g F_g \approx \sigma_F^+ F^+ - \sigma_F^- F^-. \quad (27)$$

Here,

$$\sigma_F^\pm \equiv \frac{\sum_{g=1}^G \sigma_g F_g^\pm}{\sum_{g=1}^G F_g^\pm}, \quad (28)$$

$$F_g^\pm \equiv \sum_{\mu_m \gtrless 0} \mu_m I_{g,m} w_m, \quad (29)$$

$$F^\pm \equiv \sum_g F_g^\pm. \quad (30)$$

The σ_F^\pm are well defined since $F_g^\pm > 0$ for any realistic problem. However, because we are introducing new variables (F^\pm) into the LO system, additional inexact equations are required to close the LO system. One possibility is as follows:

$$F^\pm = \alpha^\pm E \pm \frac{1}{2} F, \quad (31)$$

where the α^\pm are calculated from the HO solution. However, in our investigations, we found that this results in a method with the same instability issues as the original HOLO method. It is possible that there exists a better method of closing the system that would make the method stable, but we have not found one at this time.

Lastly, we consider a “hybrid” opacity, $\tilde{\sigma}_F$, that limits to σ_R as $F_g \rightarrow 0$ and limits to σ_F for $|F_g| \gg 0$. $\tilde{\sigma}_F$ is constructed to incorporate the accuracy and consistency of σ_F while maintaining the stability and robustness of σ_R as $F_g \rightarrow 0$. For example, one

may define $\tilde{\sigma}_F$ as follows:

$$\tilde{\sigma}_F \equiv \frac{\sum_g \left[e^{\frac{-|F_g|}{zB_g}} \left[\frac{2}{3\sigma_g} \frac{\partial B_g}{\partial x} \right] + \left[1 - e^{\frac{-|F_g|}{zB_g}} \right] F_g \right] \sigma_g}{\sum_g \left[e^{\frac{-|F_g|}{zB_g}} \left[\frac{2}{3\sigma_g} \frac{\partial B_g}{\partial x} \right] + \left[1 - e^{\frac{-|F_g|}{zB_g}} \right] F_g \right]}, \quad (32)$$

where z is a positive scaling factor. Since $\tilde{\sigma}_F$ limits to σ_R as $F_g \rightarrow 0$, its stability profile is identical to that of σ_R for our linearized, near-equilibrium stability analysis. In Equation (32), we have imposed an energy shape on σ_F as $F_g \rightarrow 0$ (an energy shape that is consistent with the Rosseland opacity), but the validity of this choice is unclear. Moreover, it is unclear how “fast” $\tilde{\sigma}_F$ should transition from σ_F to σ_R and where this transition should occur. In the above definition of $\tilde{\sigma}_F$, the parameter z controls this transition, and it is not obvious what z should be.

Many questions remain unanswered regarding the viability of alternatives to using σ_R . Nonetheless, alternatives such as those discussed in this section may be an important area of future study for optimizing the accuracy and robustness of the HOLO method.

3. Linear stability analysis of the modified predictor-corrector HOLO method

3.1. Ansatz

In this section, we repeat the linear stability analysis done by Haut et al. (2015), but for the HOLO-R method instead of the original HOLO method. We note that this analysis is done for a 2-group problem, with constant, temperature-independent absorption opacities. As noted by Haut, Equations (8)–(25) permit the equilibrium solution

$$T^n = T_0, \quad I_{g,m}^n = 2\pi B_{g0} \equiv 2\pi B_g(T_0), \quad E^n = \frac{4\pi}{c} [B_{10} + B_{20}], \quad F^n = 0. \quad (33)$$

To perturb the system about the equilibrium solution, we use the following ansatz (Equations 26–33 of Haut’s paper):

$$T^{n+1/2}(x) = T_0 + \epsilon \hat{M}_0 \omega^n e^{i\xi x} + O(\epsilon^2) \quad (34a)$$

$$T^n(x) = T_0 + \epsilon \hat{M}_1 \omega^n e^{i\xi x} + O(\epsilon^2), \quad (34b)$$

$$E^{n+1/2}(x) = \frac{4\pi}{c} [B_{10} + B_{20}] + \epsilon \hat{K}_0 \omega^n e^{i\xi x} + O(\epsilon^2), \quad (34c)$$

$$E^n(x) = \frac{4\pi}{c} [B_{10} + B_{20}] + \epsilon \hat{K}_1 \omega^n e^{i\xi x} + O(\epsilon^2), \quad (34d)$$

$$F^{n+1/2}(x) = \epsilon \hat{L}_0 \omega^n e^{i\xi x} + O(\epsilon^2), \quad (34e)$$

$$F^n(x) = \epsilon \hat{L}_1 \omega^n e^{i\xi x} + O(\epsilon^2), \quad (34f)$$

$$I_{g,m}^n(x) = 2\pi B_{g0} + \epsilon \hat{J}_{g,m} \omega^n e^{i\xi x} + O(\epsilon^2). \quad (34g)$$

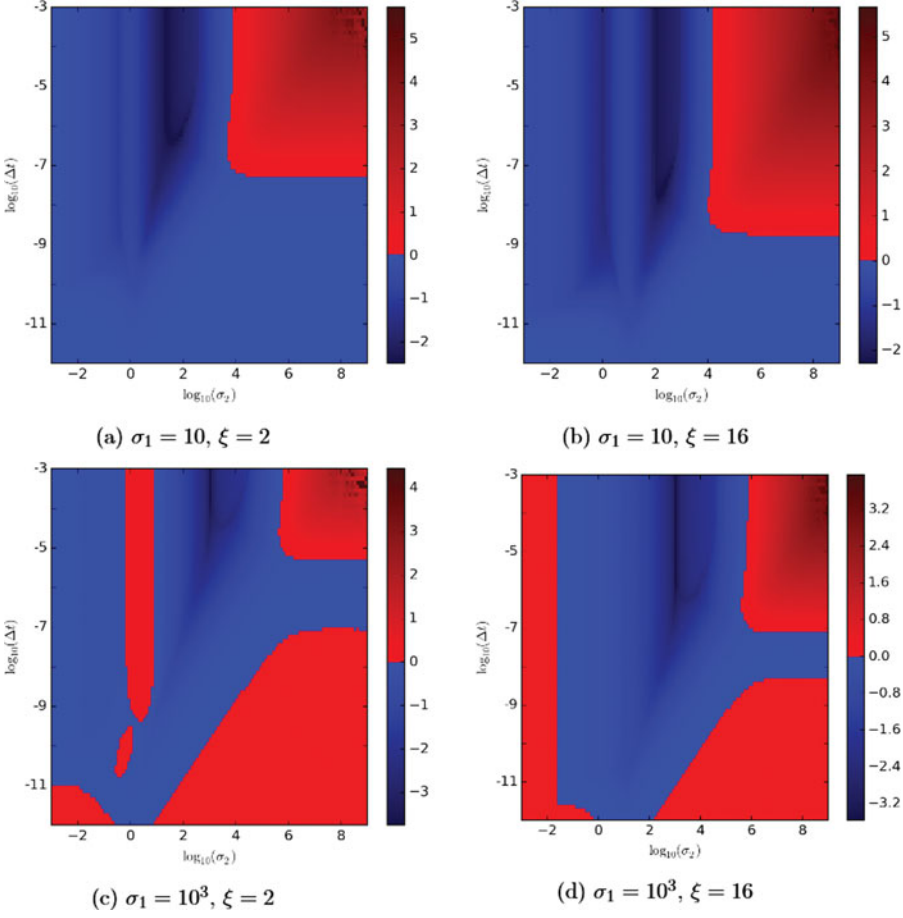


Figure 1. $\log_{10} |\omega_{\max}|$ vs. σ_2 and Δt , for $\sigma_1 = [10, 10^3]$ and $\xi = [2, 16]$ for the original HOLO method, taken from Figure 1 of Haut's paper (Haut et al., 2015). This figure should be compared to Figure 3.

Here, ϵ is an arbitrary, nondimensional parameter used to perturb the equilibrium solution, and ξ is a tunable parameter representing the spatial frequency of the perturbation. Other tunable parameters include T_0 , c_b , σ_g , ν_g , and Δt . Substituting Equations (34) into Equations (8)–(25) and ignoring all terms of $O(\epsilon^2)$ results in a homogeneous, linear system of $2M + 3$ equations whose eigenvalues are the amplification/decay factors ω . The quantity of interest is the maximum value of $|\omega|$, which should be less than 1 to ensure stability. The algebraic details of this process are omitted from this paper, but can be found in Haut et al. (2015).

3.2. Stability results

Our stability analysis for HOLO-R covered the same parameter space as that covered by Figures 1(a)–(d) and 2(a)–(d) of Haut's paper. In this section, unless otherwise noted, $T_0 = 200$, $\nu_g = [0, 100, \infty]$, $c_b = 10$, and units are such that $h = 3.53191 \cdot 10^{-11}$ and $c = 3 \cdot 10^{10}$.

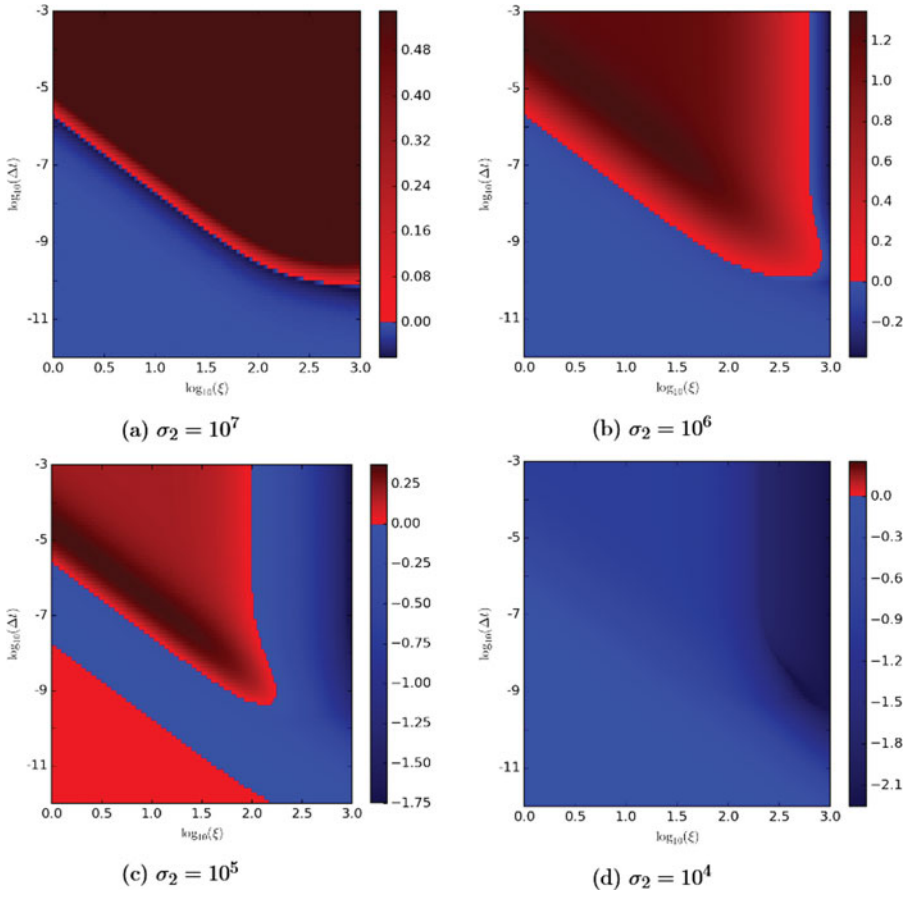


Figure 2. $\log_{10} |\omega_{\max}|$ vs. ξ and Δt , for $\sigma_1 = 10^2$ and $\sigma_2 = [10^4, 10^5, 10^6, 10^7]$ for the original HOLO method, taken from Figure 2 of Haut's paper (Haut et al., 2015). This figure should be compared to Figure 4.

Figures 1(a)–(d) and 2(a)–(d) of Haut's paper, which plot the maximum value of $|\omega|$ over a large multidimensional parameter space for the original HOLO method, are reproduced in this paper. Here, they are also labeled as Figures 1(a)–(d) and 2(a)–(d). Next, Figures 3 and 4 explore the same parameter space as Figures 1 and 2, but for the HOLO-R method instead of the HOLO method. In all of these stability plots, $\log_{10} \omega_{\max} = \log_{10} (\max |\omega|)$ is shown using a discontinuous color map – unstable regions are highlighted in red, while stable regions ($\omega_{\max} < 1$) are shown in blue.

In Figures 1 and 3, we plot ω_{\max} as a function of Δt and σ_2 , for $\sigma_1 = [10, 10^3]$ and $\xi = [2, 16]$. We sample $\log_{10} \Delta t$ and $\log_{10} \sigma_2$ at intervals of 0.1. In Figures 2 and 4, we fix $\sigma_1 = 10^2$ and plot ω_{\max} as a function of Δt and ξ for $\sigma_2 = [10^4, 10^5, 10^6, 10^7]$. Here, we sample $\log_{10} \Delta t$ and $\log_{10} \xi$ at intervals of 0.1 and 0.025, respectively. We see that HOLO-R (Figures 3 and 4), unlike HOLO (Figures 1 and 2), has $\omega_{\max} < 1$ for all of the parameter space considered. This strongly suggests that HOLO-R is unconditionally stable, as the parameter space considered here is fairly exhaustive. We used a modified version of the Mathematica script that Haut used in his paper to generate the results in Figures 3 and 4. Interestingly, many of the contours that exist

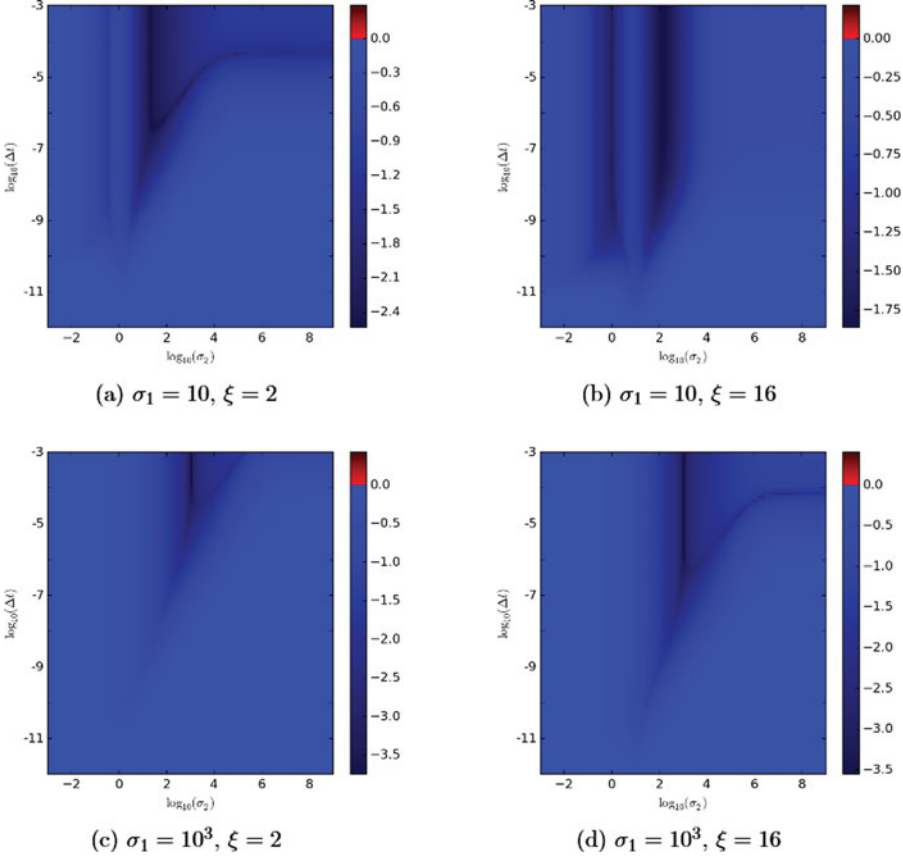


Figure 3. $\log_{10} |\omega_{\max}|$ vs. σ_2 and Δt , for $\sigma_1 = [10, 10^3]$ and $\xi = [2, 16]$ for the HOLO-R method. This figure should be compared to Figure 1.

in Figures 1 and 2 are present in Figures 3 and 4, but with a different magnitude. That is, only the magnitude of $|\omega_{\max}|$ seems to have changed from the original HOLO method to HOLO-R – the shape of $|\omega_{\max}|$ as a function of the input parameters is still roughly the same.

3.3. Verification of stability results with a spectral HOLO code

In Haut’s paper, the theoretical (predicted) values of $|\omega_{\max}|$ from the stability analysis are verified using a S_N HOLO code with a spectral spatial discretization. We have modified Haut’s spectral code so that it uses HOLO-R instead of HOLO, and, here, we use it to verify the stability analysis for HOLO-R. For a problem with periodic boundary conditions, and

$$\begin{aligned} T_0 &= 200 \text{ eV}, \quad \nu_g = [1, 100, 10^4] \text{ eV}, \quad c_v = 1.023 \cdot 10^{12} \text{ erg}/(\text{cm}^3 \text{ eV}), \\ \sigma_g &= [10, 5] \text{ cm}^{-1}, \quad \Delta t = 5 \cdot 10^{-10} \text{ s}, \end{aligned} \quad (35)$$

we perturb the equilibrium solution by $\frac{T_0}{100} \cos(2x)$, so that $\xi = 2$ (Haut et al., 2015). Moreover, we use the S_8 Gaussian quadrature set and $N_x = 40$ spatial cells

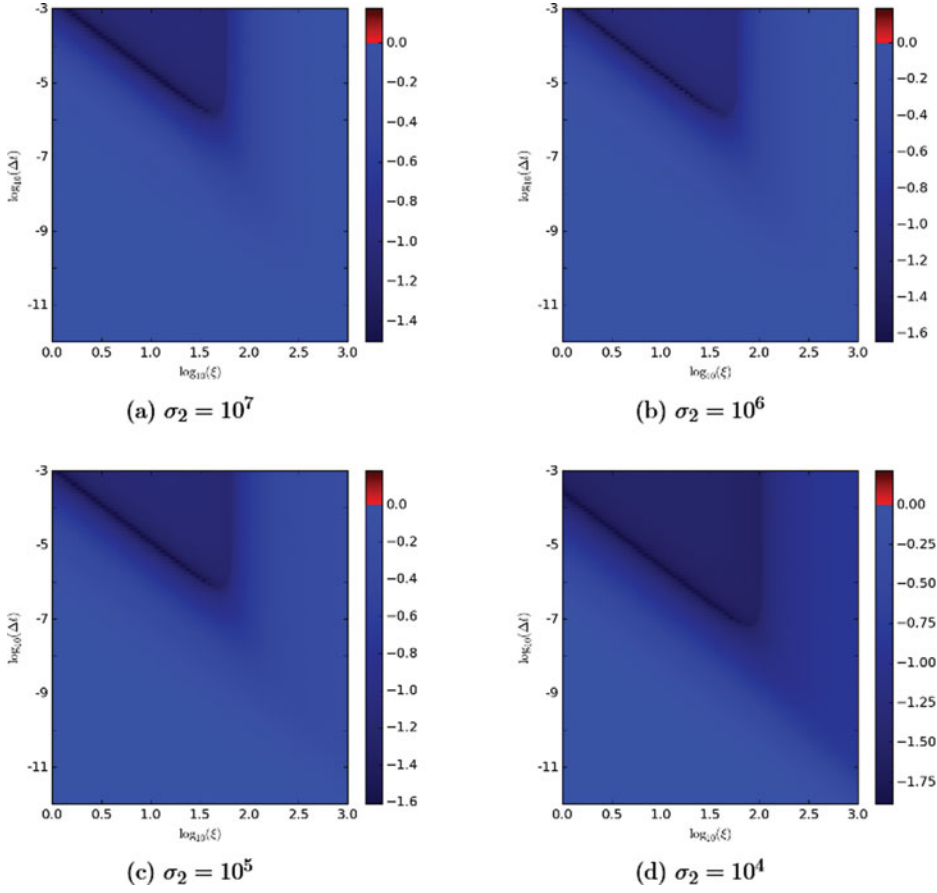


Figure 4. $\log_{10} |\omega_{\max}|$ vs. ξ and Δt , for $\sigma_1 = 10^2$ and $\sigma_2 = [10^4, 10^5, 10^6, 10^7]$ for the HOLO-R method. This figure should be compared to [Figure 2](#).

to cover a spatial region spanning two periods ($0 \leq x \leq 2\pi$). For HOLO-R, Haut's spectral code produces $\omega_{\max} = 0.984615$, while the stability analysis produces $\omega_{\max} = 0.984622$. As in Haut's paper, the theoretical and numerical results agree to nearly 5 digits. Moreover, we note that the decay rate for this particular problem is nearly identical to that of the original HOLO method. (See Figure 4 of Haut's paper.) Next, we consider a problem from Haut's paper that was unstable with the original HOLO method. This problem is identical to the previous problem, except for

$$\sigma_g = [10^7, 10^2] \text{ cm}^{-1}, \Delta t = 10^{-9} \text{ s}, N_x = 100. \quad (36)$$

For the remainder of this paper, we will refer to this problem as the Haut5b problem (since the results are plotted in Figure 5b of Haut's paper). Unlike HOLO, HOLO-R is stable for the Haut5b problem. For HOLO-R, the spectral code produces $\omega_{\max} = 0.998308$, while the stability analysis from [Section 3.2](#) yields $\omega_{\max} = 0.998295$. [Figure 5](#) contrasts the unstable results from the original HOLO method with the stable results from the HOLO-R method. Though not explicitly shown in the figures, the oscillations in the original HOLO results grow as n increases until Newton's method fails to converge at $n \approx 80$.

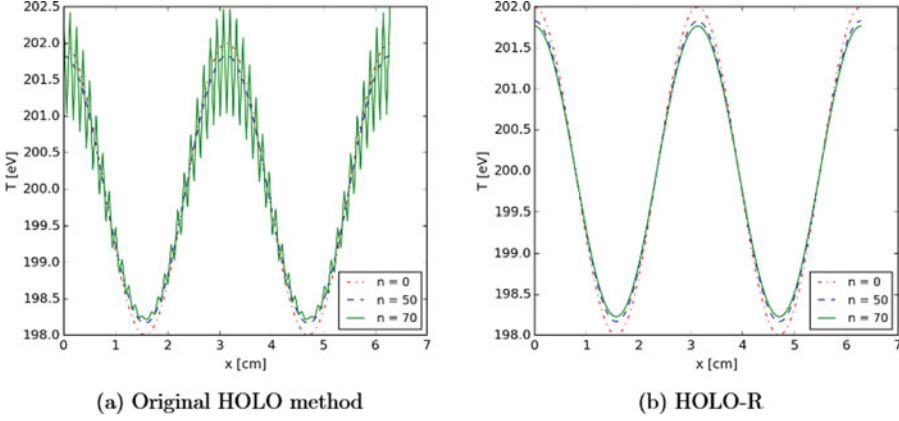


Figure 5. Plots of the material temperature profile $T(x)$ at various time steps n for the Haut5b problem from Section 3.2. The plot on the right is generated by a modified version of Haut’s spectral code (Haut et al., 2015), while the plot on the left is identical to Figure 5(b) in Haut’s paper.

We note that this analysis has not been extended to temperature-dependent opacities, but we do consider a Marshak wave problem with temperature-dependent opacities in Section 4.2.2. From our results, it does not appear that the introduction of temperature-dependent opacities causes any stability issues, but future work should include a more thorough analysis of this.

4. Implementation of HOLO-R with discontinuous Galerkin

4.1. Implementation details

The second part of this paper discusses the results from our implementation of HOLO-R in the Capsaicin code. Capsaicin is a deterministic, discrete-ordinates code developed by Los Alamos National Laboratory for solving neutron transport and TRT problems (Thompson et al., 2005). In Capsaicin, the HO and LO systems of HOLO-R are discretized with a mass-lumped DG spatial discretization scheme (Reddy, 1993). This is the first time that a DG spatial discretization scheme has been used for both the HO and LO systems.

Due to the discontinuous and upwinded nature of the HO solution in a DG spatial discretization, extra care must be taken to ensure that the boundary terms in the LO system are consistent with the HO system. The boundary terms arising from an integration-by-parts of the spatial derivatives of E and F in the LO system must be replaced with incoming and outgoing partial fluxes (F^\pm). The outgoing partial fluxes are computed using quantities from the current cell, while the incoming partial fluxes are computed using quantities from neighboring cells.

However, the introduction of partial fluxes results in extra variables. Since our LO system only consists of three equations, we are only able to solve for three variables – E , F , and T . To close the system, we relate the F^\pm to E and F by

$$F^\pm = \alpha^\pm cE \pm \frac{1}{2}F, \quad (37)$$

where α^\pm is computed from the HO solution. The reader may recall that we tried using a similar expression to close the LO system for the σ_F^\pm idea in [Section 2.2](#). Interestingly, while using Equation (37) to replace the F^\pm in the collision term of the 1st angular moment equation resulted in an unstable HOLO method, using Equation (37) to replace the F^\pm in the DG boundary terms does not cause the HOLO-R method to be unstable. It is not clear at this time why this is the case.

The HO system is solved using a standard S_N source iteration algorithm, while the LO system is solved with a Jacobian–Free–Newton–Krylov (JFNK) method (Brown and Saad, 1990; Knoll and Keyes, 2004). Details on the use of JFNK and nonlinear elimination in solving the LO system are provided in a previous HOLO paper (Park et al., 2013). For the full details on implementing HOLO-R using DG for both the HO and LO systems, see [Appendix A](#).

Next, we present results for two problems from the HOLO-R implementation in Capsaicin. The first problem is the Haut5b problem from [Section 3.2](#). We will use this to show that the stability of the HOLO-R method is generally unaffected by the choice of spatial discretization. The second problem is a 50-group 1D Marshak wave problem with temperature-dependent opacities that will be used to assess the accuracy and efficiency of HOLO-R.

4.2. Results

4.2.1. Haut5b problem

In this section, we verify the Capsaicin implementation against the spectral code from [Section 3.3](#). [Figure 6\(a\)](#) shows the results for the Haut5b problem using the Capsaicin implementation of HOLO-R, while [Figure 6\(b\)](#) plots the decay of the temperature perturbation for both the spectral and Capsaicin codes as a function of time. The difference between the solutions primarily arises from differences in spatial discretization – both exhibit errors due to the finite size of the spatial cells used. A DG discretization, consisting of only linear basis functions, cannot perfectly

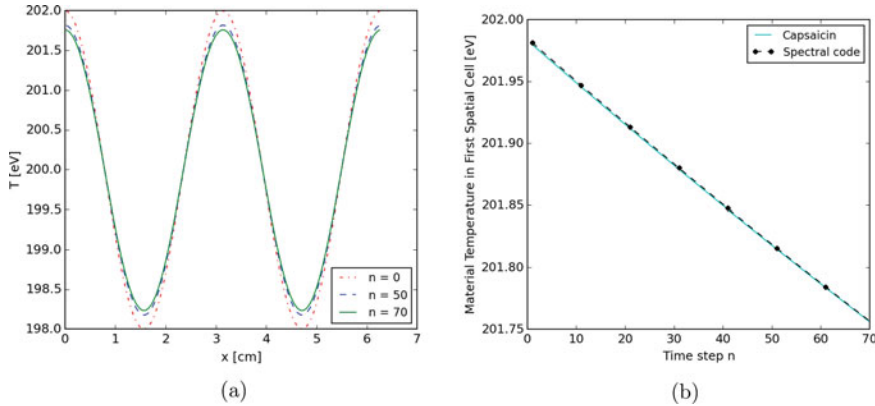


Figure 6. Results from the HOLO-R method in Capsaicin for the Haut5b problem from [Section 3.2](#). (a) $T(x)$ for various values of n . (b) Average material temperature in the first spatial cell.

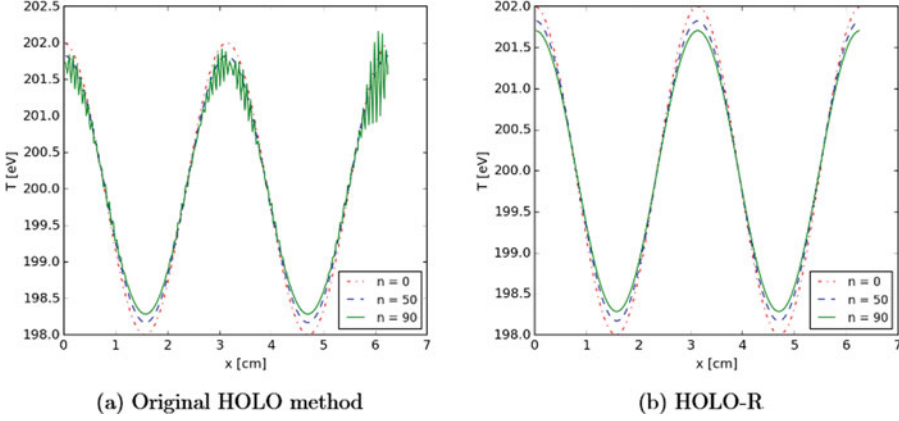


Figure 7. Material temperature profiles $T(x)$, at various time steps n , from Capsaicin for the 2-group Haut5b problem from Section 3.2 (with $N_x = 170$ instead of 100).

represent a cosine input. Moreover, a minor difference can exist due to the treatment of the boundary conditions. While the spectral code is perfectly periodic, Capsaicin uses reflective boundary conditions on both sides. In theory, this is equivalent to having periodic boundary conditions when we iterate to convergence, but, in practice, errors on the order of the convergence criterion may exist. Nonetheless, despite these differences, we see in Figure 6(b) that the results from Capsaicin and Haut's spectral code agree very well.

Interestingly, the original HOLO method, with a DG discretization, did not produce instabilities for the Haut5b problem from Section 3.2. As noted in Haut's paper (Haut et al., 2015), instabilities only appear if the mesh is fine enough to resolve the unstable modes. Clearly, the mesh size needed to resolve the unstable modes depends on the spatial discretization scheme used. For our implementation of HOLO in Capsaicin using DG, an increase of N_x from 100 to 170 is needed to resolve the unstable mode in the Haut5b problem. This instability is shown in Figure 7(a). In this figure, we see that errors on the boundary are amplified and propagated by the original HOLO method. As noted in the previous paragraph, Capsaicin uses reflective boundary conditions in place of periodic boundary conditions and, even upon convergence, very small errors can exist. These errors seed an unstable mode that is no longer periodic. As in the spectral code, the oscillations from the unstable mode grow as n increases and eventually cause the JFNK solver to fail to converge. In Figure 7(b), we see that HOLO-R remains stable for $N_x = 170$.

Next, we modify the Haut5b problem again in order to study the stability of the method for problems with more than two groups. The modifications are

$$\sigma(v) = \frac{10 \text{ cm}^{-1} \text{ eV}^3}{v^3}, \quad v_g = [1, 5, 100, 10^4] \text{ eV}, \quad \sigma_g \equiv \sigma(\sqrt{v_{g-1} v_g}), \quad N_x = 200. \quad (38)$$

In Figure 8, we contrast the results between HOLO-R and the original HOLO method. Here, we have another set of results – this time with three groups instead of two – showing that HOLO-R is stable in a regime where the original HOLO method

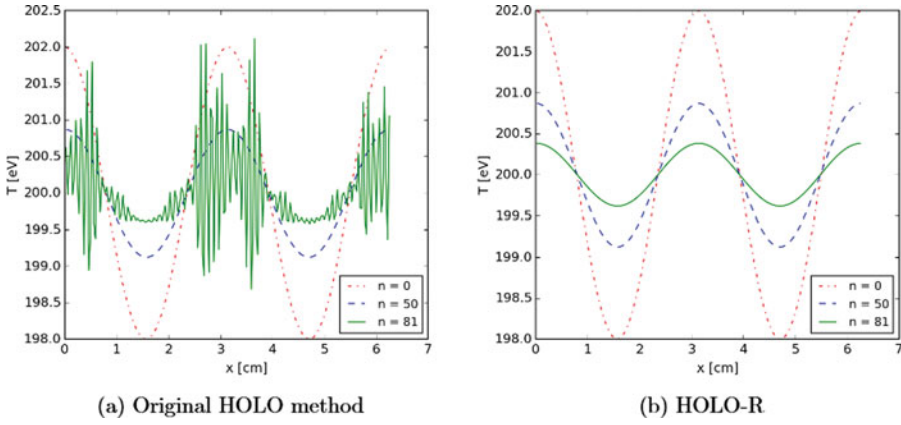


Figure 8. Material temperature profiles $T(x)$, at various time steps n , from Capsaicin for the 3-group Haut5b problem whose details are described by Equation (38).

is not. Although not conclusive, these results, along with the fact that the number of groups appears to play a minor role in the stability analysis, suggest that the HOLO-R method will remain stable for problems with arbitrary numbers of HO groups.

4.2.2. Marshak wave problem

In this section, we study the results for a multifrequency, multiregion 1D Marshak wave problem (Chang, 2007). We use 50 groups uniformly spaced between 10^{-2} and 10^4 eV in log-scale and the S_{64} Gaussian quadrature set. Compared to the Haut5b problem, this Marshak wave problem is more realistic and more complex. The opacity is given by

$$\sigma(\nu, T) = \alpha \frac{1 - e^{-\nu/T}}{\nu^3}, \quad (39)$$

where

$$\alpha = \begin{cases} 10^9 \text{ eV}^3/\text{cm}, & 0 < x < 1.0 \text{ cm}, \\ 10^{12} \text{ eV}^3/\text{cm}, & 1.0 < x < 2.0 \text{ cm}, \\ 10^9 \text{ eV}^3/\text{cm}, & 2.0 < x < 4.0 \text{ cm}. \end{cases} \quad (40)$$

As in Equation (38), the group-wise opacities σ_g are obtained by evaluating σ at the geometric mean of the group boundaries. Moreover, we have $c_v = 5.109 \cdot 10^{11}$ erg/eV-cm, and we divide the 4-cm wide domain into 80 spatial cells. The problem begins with flat material and radiation temperature profiles at 1 eV. A boundary source of 1 keV is placed at $x = 4.0$ cm, while the left boundary is vacuum. Results are presented for $t = 600$ ps, unless otherwise noted.

We note that the original HOLO method does not have any stability issues with this Marshak wave problem. Through the stability analysis (Section 3.2) and studies of the Haut5b problem with spectral and DG implementations of HOLO-R (Sections 3.3 and 4.2.1), we have already established that HOLO-R is significantly more stable than the original HOLO method, and that it is likely unconditionally

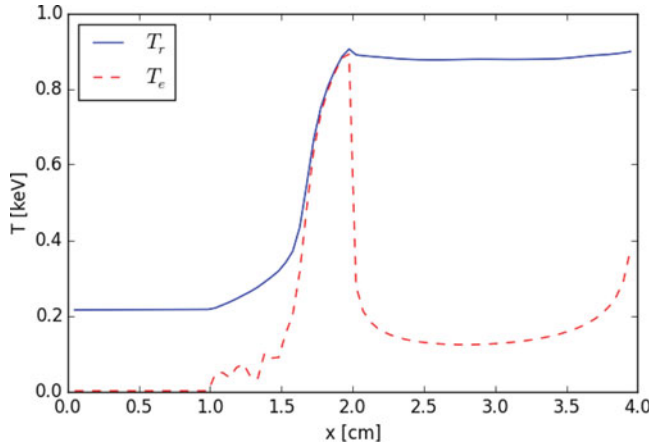


Figure 9. Radiation and material temperature profiles from the Capsaicin implementation of predictor-corrector HOLO-R for the Marshak wave problem from [Section 4.2.2](#). Here, $\Delta t = 5$ ps and results are shown for $t = 600$ ps.

stable for 1D multigroup problems. Here, we wish to perform some preliminary studies on the accuracy and efficiency of the HOLO-R method. Moreover, we wish to ensure that there are no serious repercussions from changing σ_E to σ_R in the first angular momentum equation.

[Figure 9](#) shows plots of the material and radiation temperature profiles for $\Delta t = 5$ ps using predictor-corrector HOLO-R. These plots mostly agree with results from previous papers (Park et al., 2014; Chang, 2007). The primary anomaly is the oscillation in the material temperature profile between 1.0 cm and 1.5 cm – this is a result of the HOLO-R method, and does not occur when the original HOLO method is used. We see in [Figure 10\(a\)](#) that this does not mean HOLO-R is unstable – unlike the oscillations from the original HOLO method in the Haut5b problem, the oscillations here dampen and disappear as n increases. We also see in [Figure 10\(b\)](#) that these oscillations disappear when we iterate between the HO and LO solutions, suggesting that this is mostly an issue with accuracy and consistency. Although we have

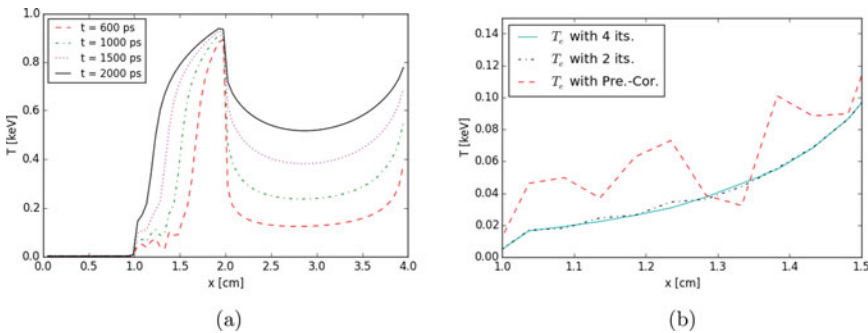


Figure 10. Plots showing the dampening of the oscillations in the material temperature profile $T(x)$ from [Figure 9](#), as we increase t or increase the number of iterations between HO and LO. (a) Predictor-Corrector HOLO-R for various times t . (b) HOLO-R solution at $t = 600$ ps for different numbers of iterations per Δt (zoomed-in).

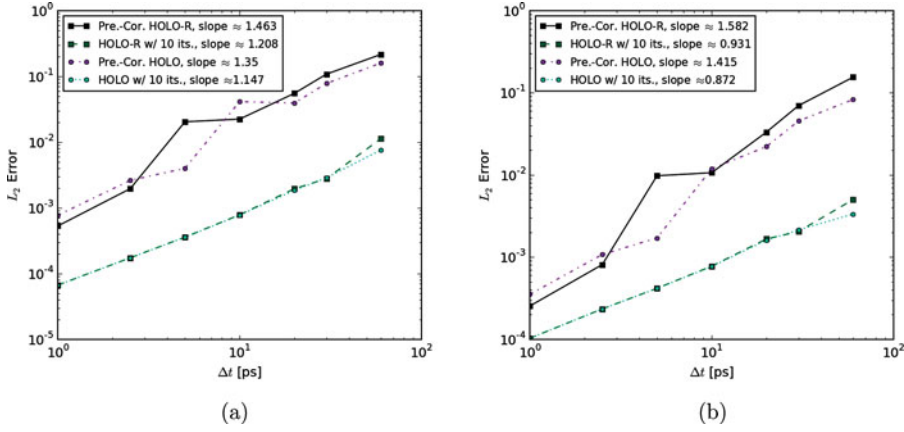


Figure 11. L_2 error vs. Δt for the predictor-corrector HOLO methods and 10-iteration HOLO methods in Capsaicin at $t = 600$ ps for the Marshak wave problem from Section 4.2.2. A reference solution is generated using the *hidalgo* package in Capsaicin with $\Delta t = 0.05$ ps. (a) L_2 error in material temperature. (b) L_2 error in radiation temperature.

shown that the HOLO-R method is stable, the unphysical oscillations in Figure 9 may cause instabilities in larger multiphysics codes where HOLO-R is coupled to other multiphysics solvers. Because of this, these oscillations should be a topic of future study. It is possible that replacing the σ_R with one of the alternatives suggested in Section 2.2, or a different definition we have not considered, will remedy this issue.

Next, we present plots profiling the accuracy of the HOLO-R method as we change Δt and the number of iterations between HO and LO. We note that a predictor-corrector method is equivalent to “1 iteration” on all of the plots in this section. A reference solution for this problem is generated using the *hidalgo* package in Capsaicin with $\Delta t = 5 \cdot 10^{-2}$ ps. The *hidalgo* package directly solves a backward Euler time discretization of the TRT equations with a nonlinear solver. *Hidalgo* uses fixed (explicit) opacities, and does not iterate on the opacity values in its nonlinear iterations.

Figure 11 shows the L_2 error in the material and radiation temperature profiles vs. Δt for four variants of the HOLO method. We see that the iterated HOLO methods are roughly first order in time – this is expected because a backward Euler time discretization has an $O(\Delta t^2)$ truncation error. Moreover, when we iterate between HO and LO, the two HOLO methods yield nearly the same results. This is because the iterations allow the γ consistency factors to converge to the correct value, making the LO systems in the two methods essentially equivalent. For the predictor-corrector methods, we see that the results are different for the two HOLO methods, but the overall accuracy is roughly the same.

Figure 11(b) also shows that, as Δt increases, iterating between the HO and LO solutions becomes more important. We see that the difference between the iterated and predictor-corrector radiation temperature profiles increases as Δt increases. Figure 12 provides more insight on this phenomenon. In these plots, we see that

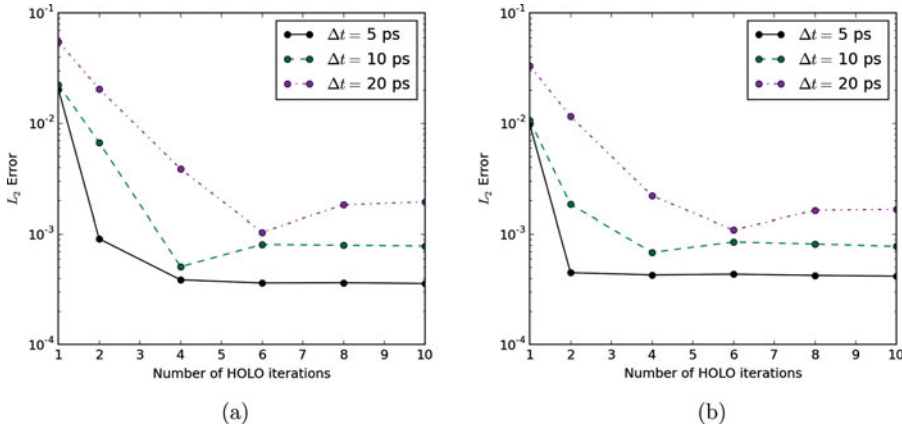


Figure 12. L_2 error vs. number of HOLO iterations per time step for HOLO-R in Capsaicin at $t = 600$ ps for the Marshak wave problem from Section 4.2.2. A reference solution is generated using the *hidalgo* package in Capsaicin with $\Delta t = 0.05$ ps. (a) L_2 error in material temperature. (b) L_2 error in radiation temperature.

the number of HOLO iterations needed to converge the consistency between the HO and LO solutions increases with Δt .

A sensitivity study has also been performed to assess the relative importance of the $(n + 1/2)$ terms that are updated with each iteration between HO and LO. In this sensitivity study, the Marshak wave problem with $\Delta t = 5$ ps was run with four iterations per time step. One of the $(n + 1/2)$ quantities is held “fixed” as the HOLO-R method iterates between HO and LO. That is, the “fixed” quantity retains its value from the first iteration between HO and LO, and maintains the value that it would have if only a predictor-corrector (1 iteration) version of the method is used. This allows us to study the convergence of the quantity after a single predictor-corrector step and the impact of further converging this quantity on the final solution.

Table 1 shows the resulting L_2 errors in material temperature at $t = 600$ ps as a result of holding various $(n + 1/2)$ quantities fixed. The “1 iteration” results should be seen as an upper bound on the error (none of the quantities were updated since no

Table 1. L_2 errors in the material temperature profile for HOLO-R with four iterations between HO and LO per time step and various quantities held “fixed.” These results are for the Marshak wave problem at $t = 600$ ps with $\Delta t = 5$ ps. Results with no quantities held fixed and results from the predictor-corrector method (i.e., 1 iteration, which is equivalent to holding all of the quantities fixed) are also provided for reference. The reference solution for the L_2 errors is generated by the *hidalgo* package in Capsaicin with $\Delta t = 0.05$ ps.

Fixed quantity	L_2 error in Mat. temp.
None (4 iterations)	$3.86 \cdot 10^{-4}$
None (1 iteration)	$2.03 \cdot 10^{-2}$
F^\pm	$3.89 \cdot 10^{-4}$
σ_R	$3.86 \cdot 10^{-4}$
σ_E	$8.76 \cdot 10^{-4}$
σ_P	$1.62 \cdot 10^{-3}$
γ	$2.88 \cdot 10^{-3}$

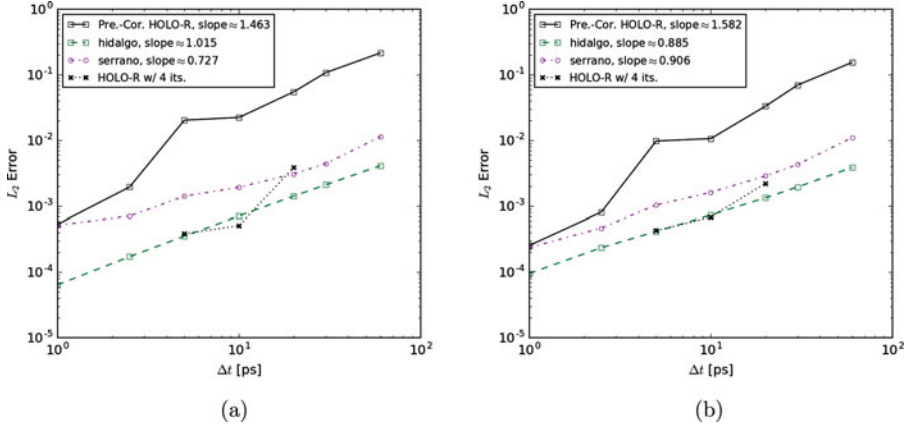


Figure 13. Comparison of the accuracy of three TRT packages in Capsaicin – predictor-corrector HOLO-R, hidalgo, and serrano. Here, the L_2 error at $t = 600$ ps of the Marshak wave problem from Section 4.2.2 is plotted at various Δt for all three methods. (a) L_2 error in material temperature. (b) L_2 error in radiation temperature.

extra HO-LO iterations are performed) and the “4 iterations” results should be seen as a lower bound (all of the quantities are updated). We note that holding the partial fluxes (F^\pm) fixed is equivalent to holding the α^\pm fixed in Equation (37). We see from Table 1 that, for this particular Marshak wave problem, the consistency terms γ have the most significant contribution, while F^\pm and σ_R have the least significance. These sensitivity results, however, are likely highly problem-dependent and the relative significance of the quantities considered in Table 1 may be different for other TRT problems. Nonetheless, the results indicate that it may be fruitful to focus future efforts on improving the definition of the γ term, especially if improved accuracy is needed for problems similar to the Marshak wave problem. Moreover, the results provide a possible explanation for the stability of the original HOLO method for this particular problem. The Rosseland opacity (σ_R) is the primary difference between the two HOLO methods, and we see in Table 1 that the convergence of this term has a relatively insignificant effect on the accuracy of the solution.

Finally, we perform a comparison between the HOLO-R method and two other TRT packages in Capsaicin – hidalgo and serrano. As we noted earlier, hidalgo directly solves the backward Euler TRT equations with a nonlinear solver. Serrano uses a Taylor series expansion of the temperature to linearize the TRT equations in a manner similar to IMC (Budge, 2004). In this paper, we solve the linear system in serrano with GMRES (Generalized Minimal Residual method) and a DSA (Diffusion Synthetic Acceleration) preconditioner. All three methods employ a lumped DG spatial discretization scheme. Figure 13 compares the accuracy of the three methods as a function of Δt . We see here that hidalgo is the most accurate since it directly solves the TRT equations. Serrano loses some accuracy due to the linearizations that it applies. Unfortunately, the predictor-corrector HOLO-R method is 1 to 2 orders of magnitude worse in accuracy than hidalgo and serrano, especially for large Δt . We note that the accuracy of the HOLO-R method can be improved at the cost of runtime by iterating between HO and LO. When we compare Figure 13

Table 2. Comparison of the runtimes for three TRT packages in Capsaicin – predictor-corrector HOLO-R, hidalgo, and serrano. Here, we report the total serial runtimes required to generate the results shown in Figure 13.

Δt (ps)	Total CPU runtime (s)		
	Pre.-Cor. HOLO-R	hidalgo	serrano
1.0	89.1	108.1	215.4
2.5	38.3	47.8	101.4
5.0	21.1	27.4	58.0
10.0	12.3	16.4	33.0
20.0	8.7	10.4	19.8
30.0	6.9	8.4	15.2
60.0	4.4	8.1	8.8

to Figure 11, we see that the accuracy for the HOLO-R method with 10 iterations is comparable to the accuracy for hidalgo. This is expected since the two systems are equivalent when the consistency terms in HOLO-R are converged.

Lastly, Table 2 provides some preliminary runtimes for the HOLO-R method and compares them to the runtimes of the hidalgo and serrano methods. We want to emphasize the preliminary nature of these runtimes. At this time, the current HOLO-R implementation in Capsaicin is fairly crude and has not been optimized for speed. Moreover, the convergence criterion for the JFNK solver for the LO system has not been optimized – in many of the cases, the solution is converged further than it needs to be. For now, the convergence criterion is set so that the JFNK solver stops when the residual is 10^{-8} times the original residual. In a few cases (especially where Δt is large), this is necessary to ensure that the convergence of the JFNK solver at later time steps but, in most cases, a smaller tolerance produces the same solution.

Overall, we see that, in generating the points in Figure 13, the predictor-corrector HOLO-R method was the fastest while serrano was the slowest. Serrano is slow because of the large amount of effective scattering generated in this Marshak wave problem, and is not an efficient choice for problems like this. Although the predictor-corrector HOLO-R method had smaller runtimes than the hidalgo method, the speedup shown in Table 2 is not enough to justify the difference in accuracy between the HOLO-R and hidalgo results. This should be primarily because of the suboptimal implementation of the HOLO-R method, as previous work has claimed significant speedups with HOLO methods over traditional methods (Densmore et al., 2015). Future work will include optimizing the HOLO-R implementation and performing a more thorough and accurate assessment of the efficiency of HOLO-R. Nonetheless, it is important to note that the HOLO-R method provides significant advantages in robustness over methods such as hidalgo and serrano. While the HOLO-R method is able to produce solutions for arbitrarily large Δt , hidalgo fails to converge for $\Delta t > 100$ ps and the serrano method fails to converge for $\Delta t > 500$ ps.

Table 3 provides preliminary runtimes for the HOLO-R method as the number of HO-LO iterations per time step is increased for $\Delta t = 5$ ps. The runtime is a slightly

Table 3. Runtimes for the HOLO-R method in Capsaicin vs. the number of HO-LO iterations used per time step. This results shown here are for the Marshak wave problem run until $t = 600$ ps, with $\Delta t = 5$ ps.

HO-LO iterations per Δt	Total CPU runtime (s)
1	21.1
2	33.6
4	59.3
6	95.0
8	125.6
10	157.8

sublinear function of the number of iterations between the HO and LO at each time step. The sublinearity is primarily due to the predictor step that is taken once at the beginning of the time step regardless of the number of iterations between the HO and LO systems. Although Figure 12 shows that running HOLO-R with six or more HO-LO iterations per time step produces an answer that is of comparable accuracy to hidalgo, we see in Table 3 that, with the current preliminary implementation of the code, it is more costly in terms of runtime. Moreover, as Δt increases, the number of HO-LO iterations needed to produce an answer of comparable accuracy to hidalgo will increase. Future work will include the optimization of the tradeoff between accuracy and computational cost that occurs when extra iterations between the HO and LO systems are taken.

5. Possible extensions to acceleration methods for neutron transport

As a final thought, we would like to note the parallels and differences between the stability issues discussed in this paper and those studied by the neutron transport community. In this paper, the stability discussed refers to the stability of the time-integration of the TRT equations. In the neutronics community, a lot of current research focuses on the stability of acceleration schemes, such as CMFD (Coarse-Mesh Finite-Difference), that speed up the convergence of source iteration for solving steady-state or eigenvalue transport problems (Smith, 1983; Lee et al., 2010; Jarrett et al., 2015). There, stability refers to convergence or nonconvergence of accelerated source iteration. This acceleration is similar to iterating between HO and LO in the HOLO method. For example, CMFD iterates between a cell-centered diffusion equation, which acts as an “LO system,” and the transport equations, which act as an “HO system.” With the HOLO method, however, we have not seen any instabilities in iterating between the HO and LO systems. It would be beneficial to understand why the HO-LO iterations appear to be unconditionally stable while CMFD-like acceleration schemes are sometimes unstable.

Moreover, one could cast the time step integration in the HOLO method as a combination of source iteration and CMFD-like steps in solving a steady-state transport problem. The term in the discretized time derivative containing the previous solution ($I^{n-1}/\Delta t$) acts as an additional source, and the absorption and re-emission of photons by the material in the TRT equations can be viewed as a form of scattering.

In this sense, it is possible that some of the insight gained from stabilizing the time integration for the HOLO method can be used to produce more stable and efficient acceleration schemes for source iteration in neutron transport problems.

6. Conclusion

We have presented a modified HOLO method (HOLO-R) that no longer has the stability issues seen in previous HOLO methods. A linear stability analysis of HOLO-R indicates that the method is likely unconditionally stable, as no regions of instability appeared in the vast parameter space considered. These stability results are supported by results from implementations of HOLO-R in a spectral code and in Capsaicin.

We have also described the implementation of HOLO-R in Capsaicin. In Capsaicin, both the HO and LO systems are discretized with DG and this is the first time that such a discretization scheme has been used for the HOLO method. Numerical results from Capsaicin show that the accuracy of the HOLO-R method is comparable to that of the original HOLO method, but with improved stability. However, HOLO-R may be more prone to results with damped spatial oscillations. A preliminary comparison to other TRT packages in Capsaicin shows that, while HOLO-R provides significant improvements in robustness, more work needs to be done to optimize the coding implementation of the method.

In addition to optimizing the code implementation, future work will include extending our implementation and analysis of the HOLO-R method to 2D problems and problems with scattering. To improve the accuracy of the method, we will also consider improvements and alternatives to HOLO-R such as those discussed in [Section 2.2](#). Moreover, further testing needs to be done to analyze the robustness and accuracy of the method, especially in regimes that are far away from the thermal equilibrium conditions about which the linear stability analysis is performed. Lastly, as noted in the [Section 5](#), we may explore whether certain aspects of this research can be applied to stabilizing or improving acceleration schemes for neutron transport.

References

- Brown, P. N., Saad, Y. (1990). Hybrid Krylov methods for nonlinear systems of equations. *SIAM J. Sci. Statist. Comput.* 11(3):450–481.
- Budge, K. (2004). Verification of the serrano photon transport package, LA-UR-04-8664. Technical report, Los Alamos National Laboratory.
- Chang, B. (2007). A deterministic photon free method to solve radiation transfer equations. *J. Comput. Phys.* 222:71–85.
- Densmore, J., Park, H., Wollaber, A., Rauenzahn, R., and Knoll, D. (2015). Monte Carlo simulation methods in moment-based scale-bridging algorithms for thermal radiative-transfer problems. *J. Comput. Phys.* 284:40–50.
- Fleck, J., Cummings, J. (1971). Implicit Monte Carlo scheme for calculating time and frequency dependent nonlinear radiation transport. *J. Comput. Phys.* 8(3):313–342.

- Haut, T. S., Lowrie, R. B., Park, H., Rauenzahn, R. M., Wollaber, A. B. (2015). A linear stability analysis of the multigroup High-Order Low-Order (HOLO) method. In *Proceedings of the Joint International Conference on Mathematics and Computation (M&C), Supercomputing in Nuclear Applications (SNA) and the Monte Carlo (MC) Method*; Nashville, TN, April 19–23, 2015. American Nuclear Society.
- Jarrett, M., Kelley, B., Kochunas, B., Downar, T., Larsen, E. (2015). Stabilization methods for CMFD acceleration. In *Proceedings of the Joint International Conference on Mathematics and Computation (M&C), Supercomputing in Nuclear Applications (SNA) and the Monte Carlo (MC) Method*; Nashville, TN, April 19–23, 2015. American Nuclear Society.
- Knoll, D. A., Keyes, D. E. (2004). Jacobian-free Newton-Krylov methods: a survey of approaches and applications. *J. Comput. Phys.* 193(2):357–397.
- Larsen, E. W., Kumar, A., Morel, J. E. (2013). Properties of the implicitly time-differenced equations of thermal radiative transport. *J. Comput. Phys.* 238:82–96.
- Lee, M. J., Joo, H. G., Lee, D. J., Smith, K. S. (2010). Investigation of CMFD accelerated Monte Carlo eigenvalue calculation with simplified low dimensional multigroup formulation. In *Proceedings of 2010 International Conference on the Physics of Reactors*; Pittsburgh, PA, May 9–14, 2010. American Nuclear Society.
- Nowak, P. F., Nemanic, M. K. (1999). Radiation transport calculations on unstructured grids using a spatially decomposed and threaded algorithm. In *Proceedings of the International Conference on Mathematics and Computation, Reactor Physics, and Environmental Analysis in Nuclear Applications*; Madrid, Spain, September 27–30, 1999.
- Park, H., Knoll, D. A., Rauenzahn, R. M., Wollaber, A. B., Densmore, J. D. (2012). A consistent, moment-based, multiscale solution approach for thermal radiative transfer problems. *Trans. Theor. Statist. Phys.* 41:284–303.
- Park, H., Knoll, D. A., Rauenzahn, R. M., Wollaber, A. B., Densmore, J. D. (2013). An efficient and time-accurate, moment-based scale-bridging algorithm for thermal radiative transfer problems. *J. Sci. Comput.* 35(5):S18–S41.
- Park, H., Knoll, D. A., Rauenzahn, R. M., Wollaber, A. B., Densmore, J. D. (2014). Moment-based acceleration of Monte Carlo solution for multifrequency thermal radiative transfer problems. *J. Comput. Theor. Trans.* 43:314–335.
- Park, H., Wollaber, A. B., Rauenzahn, R. M., Knoll, D. A. (2015). Efficient, three-temperature, thermal radiative transfer solution via a high-order, low-order method. In *Proceedings of the Joint International Conference on Mathematics and Computation (M&C), Supercomputing in Nuclear Applications (SNA) and the Monte Carlo (MC) Method*. American Nuclear Society.
- Rathkopf, J. A., Miller, D. S., Owen, J. M., Stuart, L. M., Zika, M. R., Eltgroth, P. G., Madsen, N. K., McCandless, K. P., Nowak, P. F., Nemanic, M. K., Gentile, N. A., Keen, N. D. (2000). KULL: LLNL's ASCI inertial confinement fusion simulation code. In *PHYSOR 2000 International Topical Meeting – Advances in Reactor Physics, Mathematics and Computations into the Next Millennium*; Pittsburgh, PA, May 7–11, 2000.
- Reddy, J. N. (1993). *An Introduction to the Finite Element Method*. 2nd ed. Singapore: McGraw-Hill.
- Smith, K. S. (1983). Nodal method storage reduction by nonlinear iteration. *Trans. Am. Nucl. Soc.* 44:265.
- Thompson, K., Chang, J., Warsa, J., Budge, K. (2005). The capsaicin project, LA-UR-05-3235. Technical report, Los Alamos National Laboratory.
- Wollaber, A. B. (2016). Four decades of Implicit Monte Carlo. *Journal of Comput. Theor. Trans.* 45(1–2):1–70. DOI: 10.1080/23324309.2016.1138132
- Wollaber, A. B., Larsen, E. W., Densmore, J. D. (2013). A discrete maximum principle for the Implicit Monte Carlo equations. *Nucl. Sci. Eng.* 173(3):259–275.

Appendix. Spatial discretization of the HO and LO systems in the HOLO-R method with discontinuous Galerkin (DG)

A.1. Lumped DG representations of I , E , F , and T

For a spatial cell centered at x_i , running from $x_{i-1/2}$ to $x_{i+1/2} = x_{i-1/2} + \Delta x$, the group-wise angular intensity, scalar intensity, flux, and temperature take the form

$$I_{i,g,m}^n(x) = I_{i,g,m}^{n,0} \psi_i^0(x) + I_{i,g,m}^{n,1} \psi_i^1(x), \quad (\text{A.1})$$

$$\phi_i(x) \equiv cE(x) = \phi_i^0 \psi_i^0(x) + \phi_i^1 \psi_i^1(x), \quad (\text{A.2})$$

$$F_i(x) = F_i^0 \psi_i^0(x) + F_i^1 \psi_i^1(x), \quad (\text{A.3})$$

$$T_i(x) = T_i^0 \psi_i^0(x) + T_i^1 \psi_i^1(x), \quad (\text{A.4})$$

where $I_{i,g,m}^{n,j}$, ϕ_i^j , F_i^j , and T_i^j are coefficients (constant in space for cell i) and the ψ_i^j are the following basis functions:

$$\psi_i^0(x) = \frac{1}{2} - \frac{x - x_i}{\Delta x}, \quad (\text{A.5a})$$

$$\psi_i^1(x) = \frac{1}{2} + \frac{x - x_i}{\Delta x}. \quad (\text{A.5b})$$

In the coefficients, i refers to the spatial cell, j refers to the basis function that the coefficient multiplies, m refers to the discrete ordinate μ_m , and n refers to the time step.

Moreover, in this Appendix, we will make frequent use of the lumping approximation (Reddy, 1993):

$$\begin{aligned} \sum_{j=0}^1 \phi_i^j \int_{x_{i-1/2}}^{x_{j+1/2}} \psi_i^j(x) \psi_i^k(x) dx &\approx \phi_i^k \sum_{j=0}^1 \int_{x_{i-1/2}}^{x_{j+1/2}} \psi_i^j(x) \psi_i^k(x) dx \\ &= \phi_i^k \int_{x_{i-1/2}}^{x_{j+1/2}} \psi_i^k(x) dx = \phi_i^k \frac{\Delta x}{2}. \end{aligned} \quad (\text{A.6})$$

A.2. Lumped DG HO system

The spatially continuous S_N multigroup HO system (without scattering), with a semi-implicit time discretization (i.e., it is implicit in I , but uses the predicted B), is described by

$$\frac{1}{c\Delta t} (I_{g,m}^{n+1} - I_{g,m}^n) + \mu_m \frac{\partial}{\partial x} I_{g,m}^{n+1} + \sigma_g I_{g,m}^{n+1} = \sigma_g B_g^{n+1/2}, \quad (\text{A.7})$$

where $I_{g,m}^n$ is the angular intensity for energy group g , discrete ordinate m , and time step n , and

$$B_g \equiv \int_{\nu_{g-1}}^{\nu_g} B(\nu, T) d\nu. \quad (\text{A.8})$$

Both I and T are functions of space, and this means that B is a function of space. We consider the domain $x_{i-1/2} < x < x_{i+1/2}$. If we assume a constant cross-section

within this spatial cell, we have

$$\frac{1}{c\Delta t}(I_{g,m}^{n+1} - I_{g,m}^n) + \mu_m \frac{\partial}{\partial x} I_{g,m}^{n+1} + \sigma_{g,i} I_{g,m}^{n+1} = \sigma_{g,i} B_g^{n+1/2}. \quad (\text{A.9})$$

Before we proceed, we compute the following integrals:

$$\int_{x_{i-1/2}}^{x_{i+1/2}} I_{g,m}^n(x) \psi_i^k(x) dx = \int_{x_{i-1/2}}^{x_{i+1/2}} \sum_{j=0}^1 I_{i,g,m}^{n,j} \psi_i^j(x) \psi_i^k(x) dx \approx I_{i,g,m}^{n,k} \frac{\Delta x}{2}, \quad (\text{A.10a})$$

$$\int_{x_{i-1/2}}^{x_{i+1/2}} B_{i,g}^n(x) \psi_i^k(x) dx = \int_{x_{i-1/2}}^{x_{i+1/2}} \sum_{j=0}^1 B_{i,g}^{n,j} \psi_i^j(x) \psi_i^k(x) dx \approx B_{i,g}^{n,k} \frac{\Delta x}{2}, \quad (\text{A.10b})$$

$$\begin{aligned} \int_{x_{i-1/2}}^{x_{i+1/2}} \psi_i^k(x) \frac{\partial}{\partial x} I_{g,m}^n(x) dx &\approx I_{g,m}^n(x_{i+1/2}) \delta_{k,1} - I_{g,m}^n(x_{i-1/2}) \delta_{k,0} \\ &+ (-1)^k \frac{1}{2} [I_{i,g,m}^{n,0} + I_{i,g,m}^{n,1}]. \end{aligned} \quad (\text{A.10c})$$

We note that the lumping approximation (Equation A.6) has been applied to the first two equations and,

$$B_{g,i}^j \equiv \int_{v_{g-1}}^{v_g} B(v, T_i^j) dv. \quad (\text{A.10d})$$

To close our system, we will need to define I on the faces of each cell. We upwind the boundary values so that

$$I_{g,m}^n(x_{i+1/2}) = \begin{cases} I_{i,g,m}^{n,1}, & (\mu_m > 0), \\ I_{i+1,g,m}^{n,0}, & (\mu_m < 0). \end{cases} \quad (\text{A.10e})$$

For $\mu_m > 0$, we multiply Equation (A.9) by the basis function $\psi_i^k(x)$, integrate over the spatial cell i , and use Equations (A.10) to obtain the following:

$$\begin{aligned} \left[\left(\sigma_{g,i} + \frac{1}{c\Delta t} \right) \frac{\Delta x}{2} + \frac{\mu_m}{2} \right] I_{i,g,m}^{n+1,0} + \frac{\mu_m}{2} I_{i,g,m}^{n+1,1} &= \frac{\Delta x}{2} \sigma_{g,i} B_{i,g,m}^{n+1/2,0} \\ &+ \frac{\Delta x}{2c\Delta t} I_{i,g,m}^{n,0} + \mu_m I_{i-1,g,m}^{n+1,1}, \end{aligned} \quad (\text{A.11a})$$

$$\begin{aligned} -\frac{\mu_m}{2} I_{i,g,m}^{n+1,0} + \left[\left(\sigma_{g,i} + \frac{1}{c\Delta t} \right) \frac{\Delta x}{2} + \frac{\mu_m}{2} \right] I_{i,g,m}^{n+1,1} \\ = \frac{\Delta x}{2} \sigma_{g,i} B_{i,g,m}^{n+1/2,1} + \frac{\Delta x}{2c\Delta t} I_{i,g,m}^{n,1}. \end{aligned} \quad (\text{A.11b})$$

For a sweeper, the right-hand side contains only known values. $B^{n+1/2}$ is obtained from the LO solver, I_{i-1}^{n+1} quantities are obtained from the previous cell, and I_i^n are

known from the previous time step. For $\mu_m < 0$, we have

$$\left[\left(\sigma_{g,i} + \frac{1}{c\Delta t} \right) \frac{\Delta x}{2} - \frac{\mu_m}{2} \right] I_{i,g,m}^{n+1,0} + \frac{\mu_m}{2} I_{i,g,m}^{n+1,1} = \frac{\Delta x}{2} \sigma_{g,i} B_{i,g,m}^{n+1/2,0} + \frac{\Delta x}{2c\Delta t} I_{i,g,m}^{n,0}, \quad (\text{A.12a})$$

$$\begin{aligned} -\frac{\mu_m}{2} I_{i,g,m}^{n+1,0} + \left[\left(\sigma_{g,i} + \frac{1}{c\Delta t} \right) \frac{\Delta x}{2} - \frac{\mu_m}{2} \right] I_{i,g,m}^{n+1,1} &= \frac{\Delta x}{2} \sigma_{g,i} B_{i,g,m}^{n+1/2,1} \\ + \frac{\Delta x}{2c\Delta t} I_{i,g,m}^{n,1} - \mu_m I_{i+1,g,m}^{n+1,0}. \end{aligned} \quad (\text{A.12b})$$

A.3. Spatially continuous LO equations

The LO system, discretized in time but not space, is given by

$$\frac{\phi(x) - \phi^n(x)}{c\Delta t} + \frac{\partial}{\partial x} F(x) + \sigma_E(x)\phi(x) = \sigma_P(x)ac [T(x)]^4, \quad (\text{A.13})$$

$$\frac{F(x) - F^n(x)}{c\Delta t} + \frac{1}{3} \frac{\partial}{\partial x} \phi(x) + \sigma_R(x)F(x) - \gamma\phi(x) = 0. \quad (\text{A.14})$$

F , ϕ , and T are to be solved for. These unknown quantities (the ones without a time step superscript) are at time step $n + 1/2$ if this is a predictor step, and they are at $n + 1$ if this is a corrector step. Definitions for γ , σ_E , σ_R , and σ_P are provided in Section 2.

A.4. Lumped DG zeroth-moment equations

The continuous zeroth-moment equation, Equation (A.13), is exactly satisfied by the continuous HO solution. The discretized version of the zeroth-moment equation is also exactly satisfied by the HO solution if (1) we use the correct definitions of σ_E and σ_P , (2) we have

$$\phi_i^{n,j} = \sum_g \sum_m I_{i,g,m}^{n,j} w_m, \quad (\text{A.15})$$

$$F_i^{n,j} = \sum_g \sum_m \mu_m I_{i,g,m}^{n,j} w_m, \quad (\text{A.16})$$

and (3) we have

$$F^n(x_{i+1/2}) \equiv F_{i+1/2}^n \equiv F_{i+1/2}^{+,n} - F_{i+1/2}^{-,n} = \sum_g \sum_m \mu_m I_{g,m}^n(x_{i+1/2}) w_m. \quad (\text{A.17})$$

When we integrate from the HO system to get the discretized form of the zeroth-moment LO equation, requirements 1 and 2 follow naturally. The only tricky part is the boundary terms. Extra care must be taken to ensure that the upwinding done in the HO system is properly accounted for in the LO system. This means that the value of F at faces must draw from values of I from both sides of the face, regardless of which cell we are integrating over. The incoming part of F must use values of I from the neighboring cells, while the outgoing part of F must use I from the current cell.

The corresponding expressions to Equations (A.10) for the zeroth-moment LO equation are fairly similar:

$$\int_{x_{i-1/2}}^{x_{i+1/2}} \phi(x) \psi_i^k(x) dx \approx \phi_i^k \frac{\Delta x}{2}, \quad (\text{A.18a})$$

$$\int_{x_{i-1/2}}^{x_{i+1/2}} \sigma_P(x) ac [T(x)]^4 \psi_i^k(x) dx \approx \sigma_{P,i} ac [T_i^j]^4 \frac{\Delta x}{2}, \quad (\text{A.18b})$$

$$\int_{x_{i-1/2}}^{x_{i+1/2}} \psi_i^k(x) \frac{\partial}{\partial x} F(x) dx \approx F_{i+1/2} \delta_{k,1} - F_{i-1/2} \delta_{k,0} + (-1)^k \frac{1}{2} [F_i^0 + F_i^1]. \quad (\text{A.18c})$$

We integrate Equation (A.13) times ψ_i^0 over spatial cell i , and then apply Equations (A.18) and Equation (A.17) to get

$$\left[\left(\sigma_{E,i} + \frac{1}{c\Delta t} \right) \frac{\Delta x}{2} \right] \phi_i^0 - (F_{i-1/2}^{+,n} - F_{i-1/2}^{-,n}) + \frac{1}{2} [F_i^0 + F_i^1] = S_{E,i}^0 \frac{\Delta x}{2}, \quad (\text{A.19a})$$

where

$$S_{E,i}^k \equiv \left[\sigma_{P,i} ac (T_i^k)^4 + \phi_i^{n,k} \right]. \quad (\text{A.19b})$$

Likewise, integrating with respect to ψ_i^1 yields

$$\left[\left(\sigma_{E,i} + \frac{1}{c\Delta t} \right) \frac{\Delta x}{2} \right] \phi_i^1 + (F_{i+1/2}^{+,n} - F_{i+1/2}^{-,n}) - \frac{1}{2} [F_i^0 + F_i^1] = S_{E,i}^1 \frac{\Delta x}{2}, \quad (\text{A.19c})$$

However, we want a LO system that only depends on ϕ and F . To eliminate the partial fluxes, we make the following assertions:

$$F_{i-1/2}^+ = \alpha_{i-1/2}^+ \phi_{i-1}^1 + \frac{1}{2} F_{i-1}^1, \quad (\text{A.20a})$$

$$F_{i-1/2}^- = \alpha_{i-1/2}^- \phi_i^0 - \frac{1}{2} F_i^0, \quad (\text{A.20b})$$

$$F_{i+1/2}^+ = \alpha_{i+1/2}^+ \phi_i^1 + \frac{1}{2} F_i^1, \quad (\text{A.20c})$$

$$F_{i+1/2}^- = \alpha_{i+1/2}^- \phi_{i+1}^0 - \frac{1}{2} F_{i+1}^0. \quad (\text{A.20d})$$

The α^\pm are computed from the HO solution. Substituting Equations (A.20) into Equations (A.19) gives

$$\left[\left(\sigma_{E,i} + \frac{1}{c\Delta t} \right) \frac{\Delta x}{2} + \alpha_{i-1/2}^- \right] \phi_i^0 + \frac{1}{2} F_i^1 - \alpha_{i-1/2}^+ \phi_{i-1}^1 - \frac{1}{2} F_{i-1}^1 = S_{E,i}^0 \frac{\Delta x}{2}, \quad (\text{A.21a})$$

$$\left[\left(\sigma_{E,i} + \frac{1}{c\Delta t} \right) \frac{\Delta x}{2} + \alpha_{i+1/2}^+ \right] \phi_i^1 - \frac{1}{2} F_i^0 - \alpha_{i+1/2}^- \phi_{i+1}^0 + \frac{1}{2} F_{i+1}^0 = S_{E,i}^1 \frac{\Delta x}{2}. \quad (\text{A.21b})$$

The first two terms on the left-hand side of each equation are “within the cell” – they are along the primary diagonals of the LO system. The next two terms are “connectors” or off-diagonal terms that connect the quantities within cell i to quantities within cells $i + 1$ and $i - 1$.

A.4.1. Prescribed boundary conditions

For prescribed boundary conditions, one of the F^\pm quantities is known from the inputs. For a prescribed boundary on the left ($i = 1, j = 0$), Equation (A.21a) becomes

$$\left[\left(\sigma_{E,1} + \frac{1}{c\Delta t} \right) \frac{\Delta x}{2} + \alpha_{1/2}^- \right] \phi_1^0 + \frac{1}{2} F_1^1 = S_{E,1}^0 \frac{\Delta x}{2} + F_{1/2}^+. \quad (\text{A.22a})$$

Likewise, on the right ($i = I, j = 1$), Equation (A.21b) becomes

$$\left[\left(\sigma_{E,I} + \frac{1}{c\Delta t} \right) \frac{\Delta x}{2} + \alpha_{I+1/2}^+ \right] \phi_I^1 - \frac{1}{2} F_I^0 = S_{E,I}^1 \frac{\Delta x}{2} + F_{I+1/2}^-. \quad (\text{A.22b})$$

A.4.2. Reflective boundary conditions

For reflective boundary conditions, $F^+ = F^-$. We can set the incoming partial flux equal to the outgoing one, and the boundary term goes away. Thus, on the left and right boundaries, Equations (A.19) become

$$\left[\left(\sigma_{E,1} + \frac{1}{c\Delta t} \right) \frac{\Delta x}{2} \right] \phi_1^0 + \frac{1}{2} [F_1^0 + F_1^1] = S_{E,1}^0 \frac{\Delta x}{2}, \quad (\text{A.23a})$$

$$\left[\left(\sigma_{E,I} + \frac{1}{c\Delta t} \right) \frac{\Delta x}{2} \right] \phi_I^1 - \frac{1}{2} [F_I^0 + F_I^1] = S_{E,I}^1 \frac{\Delta x}{2}. \quad (\text{A.23b})$$

A.5. Lumped DG 1st-moment equations

We can repeat the above process to derive DG equations for Equation (A.14). First, we note that

$$\int_{x_{i-1/2}}^{x_{i+1/2}} F(x) \psi_i^k(x) dx \approx F_i^k \frac{\Delta x}{2}, \quad (\text{A.24a})$$

$$\int_{x_{i-1/2}}^{x_{i+1/2}} \gamma \phi(x) \psi_i^k(x) dx \approx \gamma_i^k \phi_i^k \frac{\Delta x}{2}, \quad (\text{A.24b})$$

$$\begin{aligned} \int_{x_{i-1/2}}^{x_{i+1/2}} \psi_i^k(x) \frac{\partial}{\partial x} \phi(x) dx &\approx \phi_{i+1/2} \delta_{k,1} - \phi_{i-1/2} \delta_{k,0} + (-1)^k \frac{1}{2} [\phi_i^0 + \phi_i^1] \\ &\approx 2 \left(F_{i+1/2}^+ + F_{i+1/2}^- \right) \delta_{k,1} - 2 \left(F_{i-1/2}^+ + F_{i-1/2}^- \right) \delta_{k,0} + (-1)^k \frac{1}{2} [\phi_i^0 + \phi_i^1]. \end{aligned} \quad (\text{A.24c})$$

Here, we have approximated the boundary scalar intensities ϕ^\pm in Equation (A.24c) with partial fluxes. The error introduced by this approximation will be compensated for by the $\gamma \phi$ term. This approximation is introduced because partial fluxes are much more readily available in the Capsaicin code than partial scalar intensities.

We note that it may be possible to improve the accuracy by using partial scalar intensities rather than partial fluxes.

Integrating Equation (A.13) with respect to $3\psi_i^0$ and $3\psi_i^1$ over spatial cell i , and using Equations (A.24), we get

$$\begin{aligned} & \left[\frac{3\Delta x}{2} \gamma_i^0 + \frac{1}{2} \right] \phi_i^0 + \frac{1}{2} \phi_i^1 + \left[\left(\sigma_{F,i} + \frac{1}{c\Delta t} \right) \frac{3\Delta x}{2} \right] F_i^0 - 2(F_{i-1/2}^+ + F_{i-1/2}^-) \\ &= \frac{1}{c\Delta t} \frac{3\Delta x}{2} F_i^{n,0}, \end{aligned} \quad (\text{A.25a})$$

$$\begin{aligned} & -\frac{1}{2} \phi_i^1 + \left[\frac{3\Delta x}{2} \gamma_i^1 - \frac{1}{2} \right] \phi_i^1 + \left[\left(\sigma_{F,i} + \frac{1}{c\Delta t} \right) \frac{3\Delta x}{2} \right] F_i^1 + 2(F_{i+1/2}^+ + F_{i+1/2}^-) \\ &= \frac{1}{c\Delta t} \frac{3\Delta x}{2} F_i^{n,1}. \end{aligned} \quad (\text{A.25b})$$

Substituting in Equations (A.20) and rearranging yields

$$\begin{aligned} & \left[\frac{3\Delta x}{2} \gamma_i^0 + \frac{1}{2} - 2\alpha_{i-1/2}^- \right] \phi_i^0 + \frac{1}{2} \phi_i^1 + \left[\left(\sigma_{F,i} + \frac{1}{c\Delta t} \right) \frac{3\Delta x}{2} + 1 \right] F_i^0 \\ & - 2\alpha_{i-1/2}^+ \phi_{i-1}^1 - F_{i-1}^1 = \frac{1}{c\Delta t} \frac{3\Delta x}{2} F_i^{n,0}, \end{aligned} \quad (\text{A.26a})$$

$$\begin{aligned} & -\frac{1}{2} \phi_i^0 + \left[\frac{3\Delta x}{2} \gamma_i^1 - \frac{1}{2} + 2\alpha_{i+1/2}^+ \right] \phi_i^1 + \left[\left(\sigma_{F,i} + \frac{1}{c\Delta t} \right) \frac{3\Delta x}{2} + 1 \right] F_i^1 \\ & + 2\alpha_{i+1/2}^- \phi_{i+1}^0 - F_{i+1}^0 = \frac{1}{c\Delta t} \frac{3\Delta x}{2} F_i^{n,1}. \end{aligned} \quad (\text{A.26b})$$

A.5.1. Prescribed boundary conditions

For prescribed boundary conditions, one of the F^\pm quantities is known from the inputs. For a prescribed boundary on the left ($i = 1, j = 0$), Equation (A.26a) becomes

$$\begin{aligned} & \left[\frac{3\Delta x}{2} \gamma_1^0 + \frac{1}{2} - 2\alpha_{1-1/2}^- \right] \phi_1^0 + \frac{1}{2} \phi_1^1 + \left[\left(\sigma_{F,1} + \frac{1}{c\Delta t} \right) \frac{3\Delta x}{2} + 1 \right] F_1^0 \\ &= \frac{1}{c\Delta t} \frac{3\Delta x}{2} F_1^{n,0} + 2F_{1/2}^+. \end{aligned} \quad (\text{A.27a})$$

Likewise, on the right ($i = I, j = 1$), Equation (A.26b) becomes

$$\begin{aligned} & -\frac{1}{2} \phi_I^0 + \left[\frac{3\Delta x}{2} \gamma_I^1 - \frac{1}{2} + 2\alpha_{I+1/2}^+ \right] \phi_I^1 + \left[\left(\sigma_{F,I} + \frac{1}{c\Delta t} \right) \frac{3\Delta x}{2} + 1 \right] F_I^1 \\ &= \frac{1}{c\Delta t} \frac{3\Delta x}{2} F_I^{n,1} - 2F_{I+1/2}^-. \end{aligned} \quad (\text{A.27b})$$

A.5.2. Reflective boundary conditions

For reflective boundary conditions, $F^+ = F^-$. Thus, on the left and right boundaries, Equations (A.25) become

$$\left[\frac{3\Delta x}{2} \gamma_1^0 + \frac{1}{2} \right] \phi_1^0 + \frac{1}{2} \phi_1^1 + \left[\left(\sigma_{F,1} + \frac{1}{c\Delta t} \right) \frac{3\Delta x}{2} \right] F_1^0 - 4F_{1/2}^- = \frac{1}{c\Delta t} \frac{3\Delta x}{2} F_1^{n,0}, \quad (\text{A.28a})$$

$$\begin{aligned} & -\frac{1}{2} \phi_I^1 + \left[\frac{3\Delta x}{2} \gamma_I^1 - \frac{1}{2} \right] \phi_I^1 + \left[\left(\sigma_{F,I} + \frac{1}{c\Delta t} \right) \frac{3\Delta x}{2} \right] F_I^1 + 4F_{I+1/2}^+ \\ & = \frac{1}{c\Delta t} \frac{3\Delta x}{2} F_I^{n,1}. \end{aligned} \quad (\text{A.28b})$$

Substituting in Equations (A.20) and rearranging yields

$$\begin{aligned} & \left[\frac{3\Delta x}{2} \gamma_1^0 + \frac{1}{2} - 4\alpha_{1/2}^- \right] \phi_1^0 + \frac{1}{2} \phi_1^1 + \left[\left(\sigma_{F,1} + \frac{1}{c\Delta t} \right) \frac{3\Delta x}{2} + 2 \right] F_1^0 \\ & = \frac{1}{c\Delta t} \frac{3\Delta x}{2} F_1^{n,0}, \end{aligned} \quad (\text{A.29a})$$

$$\begin{aligned} & -\frac{1}{2} \phi_I^1 + \left[\frac{3\Delta x}{2} \gamma_I^1 - \frac{1}{2} + 4\alpha_{I+1/2}^+ \right] \phi_I^1 + \left[\left(\sigma_{F,I} + \frac{1}{c\Delta t} \right) \frac{3\Delta x}{2} + 2 \right] F_I^1 \\ & = \frac{1}{c\Delta t} \frac{3\Delta x}{2} F_I^{n,1}. \end{aligned} \quad (\text{A.29b})$$